

# Probing Organic Thin Films by Coherent X-ray Imaging and X-ray Scattering

*Nilesh Patil<sup>†\*</sup>, Theyencheri Narayanan<sup>∧</sup>, Leander Michels<sup>‡</sup>, Eirik Torbjørn Bakken Skjønsvell<sup>‡</sup>,  
Manuel Guizar-Sicairos<sup>§</sup>, Niko Van den Brande<sup>‡</sup>, Raf Claessens<sup>‡</sup>, Bruno Van Mele<sup>‡</sup>, and Dag  
Werner Breiby<sup>Δ⊥</sup>*

<sup>†</sup>Department of Physics, Norwegian University of Science and Technology (NTNU),  
Høgskoleringen 5, 7491 Trondheim, Norway

<sup>∧</sup>ESRF – The European Synchrotron, 38043, Grenoble, France

<sup>§</sup>Paul Scherrer Institut, 5232, Villigen PSI, Switzerland

<sup>‡</sup>Physical Chemistry and Polymer Science (FYSC), Vrije Universiteit Brussels, 1050 Brussels,  
Belgium

<sup>Δ</sup>PoreLab, Department of Physics, Norwegian University of Science and Technology (NTNU),  
Høgskoleringen 5, 7491 Trondheim, Norway

<sup>⊥</sup>Department of Microsystems, University of South-Eastern Norway, Campus Vestfold, 3184  
Borre, Norway

**KEYWORDS.** Morphology, SAXS, USAXS, X-ray ptychography, P3HT, PCBM

This document is the accepted manuscript version of the following article:  
Patil, N., Narayanan, T., Michels, L., Skjønsvell, E. T. B., Guizar-Sicairos, M.,  
Van den Brande, N., ... Breiby, D. W. (2019). Probing organic thin films by coherent x-  
ray imaging and x-ray scattering. *ACS Applied Electronic Materials*, 1(7), 1787-1797.  
<https://doi.org/10.1021/acsapm.9b00324>

**ABSTRACT.** An important and integral effort towards understanding the formation and reorganization of mesoscale structures in functional organic thin films, being of fundamental importance to the development of tomorrow's green energy technologies, is the continuous sharpening of the experimental analytical tools used to observe and quantify these structures. In this study we present a combined investigation of organic thin films by small-angle X-ray scattering (SAXS) and the relatively new technique of high-resolution phase-contrast ptychographic coherent X-ray diffraction imaging (CXDI). Using poly(3-hexylthiophene) (P3HT) and [6,6]-phenyl-C<sub>61</sub>-butyric acid methyl ester (PC<sub>61</sub>BM) as a model system, we present the morphology development including phase separation in thermally annealed thin film blends. The state-of-the-art synchrotron SAXS measurements spanning a large  $q$ -range from  $2 \times 10^{-3} \text{ nm}^{-1}$  to  $6 \text{ nm}^{-1}$  elucidate the multiscale structure within the material. Because the SAXS data in-fact overlaps with microscopy length scales, it is instructive to compare the small- $q$  features of the SAXS patterns with corresponding images obtained by CXDI, as these techniques are based on the same physical interaction with the sample. While the technique of CXDI, here reaching a resolution of  $\sim 100 \text{ nm}$ , is currently too coarse to investigate the structural details at the length scale of the exciton diffusion lengths, the method proved consistent with the ultra SAXS (USAXS) data and invaluable in resolving the thin-film dimensionality influence on the USAXS analysis. Our results not only offer a quantitative model for USAXS data analysis applied to thermally annealed thin films of P3HT/PC<sub>61</sub>BM, but also indicates the future applicability of emerging X-ray imaging techniques in retrieving the morphologies of low-contrast organic materials.

## 1. INTRODUCTION.

The research into organic thin films for solar cells has steadily increased over the last two decades due to the introduction of donor-acceptor heterojunctions, which act as a dissociation site for the photogenerated excitons into separate charge carriers.<sup>1</sup> Efficient charge carrier transport to the respective electrodes is essential for a well performing solar cell.<sup>2-5</sup> For optimal charge carrier generation, the size of the nanostructured domain should be similar to the exciton diffusion length of about 10 nm.<sup>6</sup> Power conversion efficiency (PCE) values in excess of 10% have been reported.<sup>7</sup> The benchmark system for organic heterojunction thin films is the mixture of poly(3-hexylthiophene) (P3HT) and [6,6]-phenyl-C<sub>61</sub>-butyric acid methyl ester (PC<sub>61</sub>BM), which is promising for better materials stability and power-conversion efficiencies. To accomplish the objectives of high-performance and chemically stable organic solar cells, the complicated nanostructure domain formation and morphology within the thin films need to be scrutinized quantitatively, and developing refined analytical tools for this purpose is a continuous and on-going effort.<sup>8-9</sup> Post-fabrication solvent and/or thermal annealing treatments are often applied, which not only offers the possibility to investigate the time-temperature dependence of nanostructure domain growth but also provides additional tools for consistently developing optimized and well-organized morphologies.<sup>10</sup> The morphological developments caused by post-fabrication thermal annealing treatments of P3HT:PC<sub>61</sub>BM are rather distinctive – it is well known that for concentrations of PC<sub>61</sub>BM above ~20%vol, pronounced phase-separation is observed, into three phases being i) pure P3HT crystals, ii) pure PC<sub>61</sub>BM crystals and iii) a mixture of their amorphous phases.<sup>11</sup>

Thin-film morphology has been studied extensively with a wide range of microscopy and scattering methods to understand the optoelectronic properties relevant for the high-performance

polymer solar cells. Transmission electron microscopy (TEM) and scanning electron microscopy (SEM) have been employed to reveal the solvent effects on the sizes of phase separated PC<sub>61</sub>BM-rich domains.<sup>12-13</sup> Savenije et al.<sup>14</sup> showed the effects of annealing temperature on the formation of three different substructures – P3HT/PC<sub>61</sub>BM blend with PC<sub>61</sub>BM-rich clusters, a depleted region of PC<sub>61</sub>BM, and the large PC<sub>61</sub>BM single crystals. Using optical microscopy (OM), Campoy-Quiles et al.<sup>15</sup> demonstrated that the thin-film morphology consists of vertically and laterally organized phase-separated domains of crystalline P3HT and PC<sub>61</sub>BM, for slow drying, thermal annealing and vapor annealing procedures. Atomic force microscopy (AFM) studies have contributed to the understanding of morphology and charge carrier mobility in P3HT films. Kline et al.<sup>16</sup> showed that thermal annealing leads to the formation of highly ordered structure composed of nanorods in low molecular weight P3HT films with low charge carrier mobility, whereas the high molecular weight P3HT films with high charge carrier mobility had less ordered, isotropic nodule structure.

The structural heterogeneities at molecular length scales can be obtained using scanning tunneling microscopy (STM). Particularly, the direct visualization of polymer chain folding for P3HT indicate the succession of thiophene units in an all-*cis* conformation corresponding to the formation tight hair-pin folds.<sup>17-18</sup> Utilizing transmission electron tomography, the 3D morphology of P3HT/PCB<sub>61</sub>M of thin films of different thicknesses has been reported to suggest that the nanoscale organization consisting of 3D network of P3HT, with the enrichment of P3HT close to hole collecting electrode, and with the enrichment of PCBM close to electron collecting electrode, is crucial for achieving high efficiency of solar cell devices.<sup>19</sup> Synchrotron-based scanning transmission X-ray microscopy (STXM) in combination with near-edge X-ray absorption fine

structure (NEXAFS) has been also used to reveal the quantitative chemical structure with a lateral resolution of sub-10 nm.<sup>20</sup>

Small angle X-ray scattering (SAXS) is a powerful technique for studying mesoscale structures of  $\leq 1\ \mu\text{m}$  in solution or solid form. A key requirement for SAXS is sufficient electronic contrast, i.e. difference in electron density, between adjacent phases. Quantitative SAXS data analysis is often complicated for composite materials by the existence of multi-level nanostructural organization and their dispersity. Nevertheless, valuable structural information can be obtained by analyzing the measured scattered intensities in terms of an appropriate structural model. In monodisperse systems, the size and shape of the particles can be determined rather straightforwardly.<sup>21</sup> In polydisperse systems, generally it is difficult to separate size and shape distributions. In systems with a finite concentration of particles, the free-form size distribution can sometimes be determined using non-linear least-square fitting.<sup>21</sup>

SAXS and Wide angle X-ray scattering (WAXS), in particular in grazing incidence geometry (GISAXS and GIWAXS, respectively), enables the nanoscale morphology, molecular packing and preferred orientation within (semi-)crystalline domains in organic films to be studied.<sup>3, 22-25</sup> While WAXS is a crucial technique to the development of organic electronics, its low sensitivity to weakly ordered (“amorphous”) large domains is a limitation.

With the availability of high-brilliance synchrotron X-ray beamlines featuring advanced instrumentation and detectors, acquisition of high-quality scattering data down to low  $q$  ( $\sim 10^{-3}\ \text{nm}^{-1}$ ) value is now possible.<sup>26</sup> Here,  $q$  is the magnitude of the scattering vector given by  $q = (4\pi/\lambda) \sin(\theta)$ , with  $\lambda$  the X-ray wavelength and  $2\theta$  the scattering angle. In view of recent developments in synchrotron based X-ray and neutron scattering techniques, several studies are published on the modelling of small angle scattering (SAS) data for characterizing the mesoscale morphology in

P3HT/PC<sub>61</sub>BM blend thin films,<sup>27-35</sup> as well as in pure P3HT thin films.<sup>36-37</sup> These studies have typically been performed with the aim of defining the form and structure factors of phase-segregated structures in polymer-polymer and/or polymer-fullerene blend films. Generally, the average form factor describes the typical shape and size of the scattering objects, while the structure factor accounts for the spatial correlation between the scattering objects. See **Table 1** for an overview of the published literature, listing SAXS models applied to P3HT/PC<sub>61</sub>BM organic thin films.

Several recently developed X-ray microscopy techniques are useful for imaging weakly scattering materials.<sup>38-40</sup> Notably, X-ray ptychography, which is a scanning variant of coherent diffractive imaging (CDI),<sup>41-42</sup> has been used for visualization of bulk heterojunction (BHJ) morphology over large fields of view with a spatial resolution of about 100 nm.<sup>43-44</sup> X-ray ptychography is a highly promising technique for studying soft materials and polymers because it allows quantitative imaging of complex morphologies in the sample under challenging environments<sup>40, 43-47</sup> in a non-destructive manner. The ptychography method involves applying iterative reconstruction algorithms<sup>41, 48-49</sup> to a series of coherent diffraction patterns. The sample is scanned with respect to the incoming beam in such a way that a significant spatial overlap between adjacent exposures is maintained. The overlap is utilized as a constraint during the image reconstruction process to retrieve the complex-valued projection of the sample, i.e. both phase and amplitude, which are associated to the wavefront retardation and sample absorption, respectively.

In this article, a combination of ultra-small-angle X-ray scattering (USAXS), SAXS and X-ray ptychography is employed for characterizing the well-known BHJ morphology in thermally treated P3HT/PC<sub>61</sub>BM thin films. The article is organized as follows. In Section 2, the experimental details are provided. Section 3 presents USAXS and SAXS data covering a large  $q$ -range, clearly

revealing the need for an improved scattering model, and continues with a more focused discussion on the P3HT/PC<sub>61</sub>BM blends. In addition, X-ray ptychographic imaging is presented to reveal clustering of PC<sub>61</sub>BM for different thermal annealing schemes, consistent with both the USAXS results and previously reported studies based on optical microscopy, see e.g. Campoy-Quiles et al.<sup>15</sup> Furthermore, the scattering intensity  $I(q)$  was computed from the X-ray ptychographic phase-contrast projections for direct comparison with the USAXS data, emphasizing the synergy and complementarity between the two techniques. The main feature of this work is that we performed SAXS measurements over an extended range of  $q$ , covering the molecular scale to the aggregate morphology and quantitatively modeled the intensity profiles with fewer parameters. In addition, we demonstrate the complementarity with the emerging technique of X-ray ptychography, which holds promise of future nanoscale real-space imaging. The structural elucidation using X-ray imaging and scattering techniques can provide deeper understanding required for improving the performance of polymer solar cells.

**Table 1.** Different SAS models used in the literature for modelling of bulk heterojunction morphologies in P3HT/PC<sub>61</sub>BM thin films.

No.	Models used	$q$ -range / nm <sup>-1</sup>	Ref.
1.	DAB, Polydisperse HS	0.05 to 2	Liao et al. <sup>27</sup>
2.	Polydisperse HS	0.02 to 1.5	Kiel et al. <sup>28</sup>
3.	Polydisperse HS, DB, Polydisperse rod	0.04 to 1	Wu et al. <sup>29</sup>
4.	TS	0.05 to 1.5	Kozub et al. <sup>30</sup>
5.	DB, Porod, Elliptical cylinder	0.02 to 8	Yin et al. <sup>31</sup>
6.	DB	0.1 to 0.8	Chen et al. <sup>32</sup>
7.	Guinier	0.06 to 1	Chiu et al. <sup>33</sup>
8.	TS	0.1 to 1	Vajjala Kesava et al. <sup>34</sup>
9.	DAB, Polydisperse, Porod	0.04 to 2	Huang et al. <sup>35</sup>

Note: The abbreviations DAB, TS, DB and HS represent the Debye-Anderson-Brumberger, Teubner-Strey, Debye-Beuche and Hard Sphere models.

## 2. METHODS.

**2.1 Fabrication of thin films.** Thin films with a thickness of ~950 nm were fabricated by spin coating (100 rpm for 60 s) the solution mixture of P3HT (Rieke Metals,  $M_w \sim 10^5$  g mol<sup>-1</sup>,  $M_w/M_n = 2.4$ , regioregularity ~ 94%)/ PC<sub>61</sub>BM ( $M \sim 910.88$  g mol<sup>-1</sup>) (1:1, by weight) in chlorobenzene onto X-ray transparent silicon nitride (Si<sub>3</sub>N<sub>4</sub>) membranes of area  $A = 1.5$  mm  $\times$  1.5 mm. Thin films were subjected to both isothermal and non-isothermal annealing schemes using the differential scanning calorimetry (DSC) method. The experimental thermal history for isothermal annealing is summarized as follows: The samples were i) heated from 293 K to the melt at 553 K and held for 120 s to remove any initial structures, ii) cooled to the isothermal temperature of 400



K, iii) held at isothermal temperature for 60 s, 720 s and 7500 s, and iv) cooled down to the 293 K. A controlled rate of 20 K min<sup>-1</sup> was used for all heating and cooling steps throughout the thermal annealing treatments.

**2.2 SAXS measurements.** The SAXS and USAXS experiments were carried out at the ID02 beamline of the ESRF,<sup>26</sup> using an X-ray energy of 12.46 keV corresponding to  $\lambda = 0.995$  Å. Several sample-to-detector distances ( $d = 31.0$  m, 10.0 m and 1.0 m) were used to cover the wide  $q$ -range of more than three orders of magnitude, from 0.002 nm<sup>-1</sup> to 6 nm<sup>-1</sup> corresponding to nominal real space dimensions from about 3  $\mu$ m down to 1 nm, surpassing all previously reported SAXS studies of P3HT/PC<sub>61</sub>BM, cf. **Table 1**. Two-dimensional scattering patterns were recorded using a Rayonix MX170 HS detector. The exposure time was 0.1 s with an incident flux of  $5 \times 10^{12}$  photons/s. The measured SAXS patterns were normalized to an absolute intensity scale (units of sterad<sup>-1</sup>) using the standard procedure which includes detector dark-image correction, division by a flat field and intensity normalization.<sup>26</sup> Subsequently, the normalized patterns were azimuthally averaged to obtain the one-dimensional scattering profile as a function of  $q$ . The background intensity was measured with a bare wafer and treated following the same procedure. The scattering profiles from different detector distances were merged together after background subtraction using the software *SAXSutilities*.<sup>50</sup>

**2.3 X-ray ptychography measurements.** Two-dimensional X-ray ptychography imaging was performed at the cSAXS beamline of the Swiss Light Source (Paul Scherrer Institut, Villigen, Switzerland) using a photon energy of 6.2 keV ( $\lambda = 0.2$  nm). A pinhole aperture of approximately 3.0  $\mu$ m diameter was utilized to define the coherent illumination. The sample was placed 4 mm downstream of the pinhole, mounted on a XYZ nPoint piezoelectric nanopositioning stage. Far-field coherent diffraction patterns were recorded with a pixelated hybrid Pilatus 2M detector<sup>51</sup> with

a pixel size of  $172\ \mu\text{m} \times 172\ \mu\text{m}$  placed 7.45 m away from the sample. A He-filled flight tube was positioned between the sample and the detector to reduce absorption and scattering by air.

The ptychographic scans were performed in a Fermat spiral pattern,<sup>52</sup> with each scan covering a field of view (FOV) of  $10\ \mu\text{m} \times 10\ \mu\text{m}$ . For the isothermally annealed thin films, an average step size of  $1\ \mu\text{m}$  and a counting time of 0.5 s for each of the 100 exposures per scan was used. For the as-cast thin film, an average step size of  $0.5\ \mu\text{m}$  and a counting time of 1.0 s for each of the 400 exposures per scan was used. The images were reconstructed using a nonlinear optimization algorithm<sup>48</sup> with 300 iterations using the central  $192 \times 192$  detector pixels of the collected diffraction patterns. Linear phase gradients in the reconstructed images were removed.<sup>53</sup> The reconstructed images shown are all based on phase contrast, as the corresponding absorption images (not shown) are featureless because of the low absorption. To estimate the spatial resolution of the ptychographic phase-contrast images, Fourier Shell Correlation<sup>54-55</sup> was applied using one-bit criteria. A spatial resolution in the range of 100-120 nm in the ptychographic reconstruction was achieved.

### 3. RESULTS AND DISCUSSION.

#### 3.1 SAXS modelling of polymer particles and fullerene aggregates in thin films.

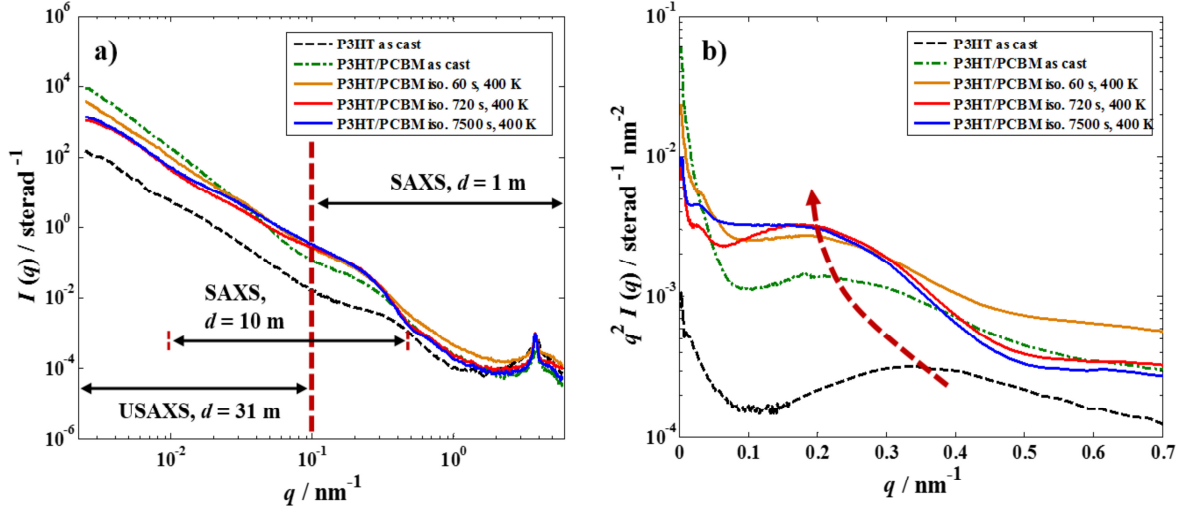


**Figure 1.** a) Absolute SAXS intensities as a function of the magnitude of scattering vector  $q$  obtained after merging data from three sample-to-detector distances for thermally treated P3HT/PC<sub>61</sub>BM thin films. b) Kratky plot of the scattering intensity at intermediate  $q$  ranges showing the shift in the peak position to lower  $q$  indicating an increase in the cross-sectional size of the scattering objects. The isothermal annealing was performed at 400 K for three different times, viz. 60 s, 720 s and 7500 s.

Figure 1 presents the absolute SAXS profiles and Kratky plot of scattering intensities for thin films subjected to different conditions. At  $q < 1 \text{ nm}^{-1}$ , the absolute scattering intensity of pure P3HT as-cast thin film, cf. **Fig. 1a**, is about an order of magnitude lower than P3HT/PC<sub>61</sub>BM thin films due to the low contrast between the crystalline and amorphous phases of the polymer. With the addition of PC<sub>61</sub>BM, contrast initially decreases to a match point and then increases.<sup>56</sup> Based on this contrast variation study<sup>56</sup> and the solution structure of P3HT,<sup>37</sup> the broad shoulder

appearing at the intermediate  $q$  range is attributed to the form factor of crystalline P3HT particles in the amorphous matrix with dispersed PC<sub>61</sub>BM. Indeed, similar sized PC<sub>61</sub>BM particles would also contribute to this feature. The contrast is significantly enhanced in the presence of denser PC<sub>61</sub>BM phase, as indicated by the higher absolute scattering cross-section for P3HT/PC<sub>61</sub>BM thin films. The higher scattering cross-section for P3HT/PC<sub>61</sub>BM thin films as compared to pure P3HT thin film for  $q < 10^{-2} \text{ nm}^{-1}$  can be further attributed to the larger size of PC<sub>61</sub>BM domains segregated in the blend since the concentration of PCBM is well above the solubility limit,<sup>56</sup> which is evident in particular for the as-cast P3HT/PC<sub>61</sub>BM thin film. The *broad* shoulder at intermediate  $q$  range, cf. **Fig. 1a**, has an inflection at  $q = 3.5 \times 10^{-1} \text{ nm}^{-1}$  for pure P3HT thin film. This inflection which appears as a peak in the Kratky plot (**Fig. 1b**) shifts to lower  $q = 2.1 \times 10^{-1} \text{ nm}^{-1}$  in as-cast P3HT/PC<sub>61</sub>BM thin film, suggesting an increase in the cross-section of polymer particles. With the increase in isothermal annealing time applied to the P3HT/PC<sub>61</sub>BM thin films, the peak in the Kratky plot further shifts systematically to lower  $q$  values, indicating a thickening of the polymer particles. Furthermore, additional features appear in the  $q$  range  $0.01 - 0.03 \text{ nm}^{-1}$ , suggesting an increased segregation of PC<sub>61</sub>BM.

The Guinier region of the particulate scattering merges with a power law scattering at lower  $q$  values. The power law scattering feature in blend films is attributed to the percolated domains of PC<sub>61</sub>BM in the amorphous matrix, while for pure P3HT, it is contributed by the polymer network and the interface scattering. For the annealing conditions used here, the two-dimensional USAXS patterns were isotropic and did not display any intensity streaks corresponding to crystalline facets.<sup>57</sup> This suggests absence of micron size PC<sub>61</sub>BM crystals in the film. At the high  $q$  region, both P3HT and P3HT/PC<sub>61</sub>BM films display a sharp Bragg peak which corresponds to the lamellar stacking within the P3HT particles.<sup>56, 58</sup> The width of this peak gives an independent estimate of

the thickness of the P3HT nanocrystals, notably in the lateral dimension as both P3HT<sup>59-60</sup> and P3HT/PC<sub>61</sub>BM films<sup>61</sup> are known to exhibit significant preferred orientation.

In order to quantitatively describe the different scattering features over the full  $q$  range of measurement, the experimental data were fitted, see **Fig. 2**, with the following SAXS model:

$$I(q) = F_p \langle P(q) \rangle \left[ S_p(q) + \frac{I_0}{(1 + \xi^2 q^2)^p} \right] + I(q)_{\text{Bragg}} + I_B \quad (1)$$

Here,  $F_p$  is a scaling parameter proportional to the product of the mean volume of polymer particles  $V_p$ , their volume fraction  $\phi$ , and the square of the scattering length density.  $\langle P(q) \rangle$  is the orientation- and size-averaged form factor of the particles, and  $S_p(q)$  is an effective structure factor describing the correlation between particles. Since there is no signature of a correlation peak in the  $I(q)$  data,  $S_p(q) \approx 1$ . The amplitude  $I_0$  is proportional to the number density and volume of the larger domains, the correlation length  $\xi$ , and the power-law exponent  $p$  are related to their characteristic size and morphology, respectively. A similar expression is used in the modelling of colloidal particles and their aggregates.<sup>50, 57</sup> The radius of gyration,  $R_g$ , of the domains or clusters is related to  $\xi$ , as  $R_g^2 \approx 3p\xi^2$ . The  $I(q)_{\text{Bragg}}$  term describes the Bragg peak at  $q \sim 3.8 \text{ nm}^{-1}$  and  $I_B$  is a small constant background ( $\sim 5 \times 10^{-5} \text{ sterad}^{-1}$ ). Several different geometrical shapes such as polydisperse spheres, ellipsoids and cylinders were tried for the choice of  $\langle P(q) \rangle$ . The best description was obtained with the form factor of randomly oriented cylinders,  $P_{\text{Cyl}}(q)$ , with the radius  $R$  and height  $H$  given by<sup>21</sup>

$$P_{Cyl}(q) = \int_0^{\pi/2} \left( \frac{2J_1(qR \sin \varphi)}{qR \sin \varphi} \times \frac{\sin(q(H/2) \cos \varphi)}{(q(H/2) \cos \varphi)} \right)^2 \sin \varphi d\varphi \quad (2)$$

where  $J_1(x)$  is the first order Bessel function and  $\varphi$  is the orientation angle.

In equation (1), the first term is the polydisperse cylinder model<sup>21</sup> which is used to calculate the average size of polymer particles in the thin films. The polymer particle is composed of polymer nanocrystals, confined in the amorphous network, which is approximated by a cylinder. The second term in equation (1) is the Debye-Beuche structure function,<sup>62</sup> which is used to parameterize the scattering from the network of PC<sub>61</sub>BM domains in the amorphous matrix or outside. The third term is the scattering intensity associated with the Bragg peak present in the high  $q$ -region ( $q \sim 3.8 \text{ nm}^{-1}$ ). The Bragg peak gives the  $d$ -spacing or lamellar spacing of P3HT nanocrystals. The peak profile can be fitted using the Pseudo-Voigt approximation<sup>63</sup> as

$$I(q)_{Bragg} = A_B \left[ \frac{2\mu}{\pi} \left( \frac{\sigma_L}{\sigma_L^2 + 4(q - q_c)^2} \right) + \frac{(1-\mu)}{\sqrt{\pi}} \left( \frac{\sqrt{4 \ln 2}}{\sigma_G} \exp(-4 \ln 2 (q - q_c)^2 / \sigma_G^2) \right) \right] \quad (3)$$

Here,  $\sigma_L$  and  $\sigma_G$  are the width parameters for the Lorentzian and the Gaussian terms,  $\mu$  is a relative weighting factor, and  $q_c$  is the peak value of scattering vector.

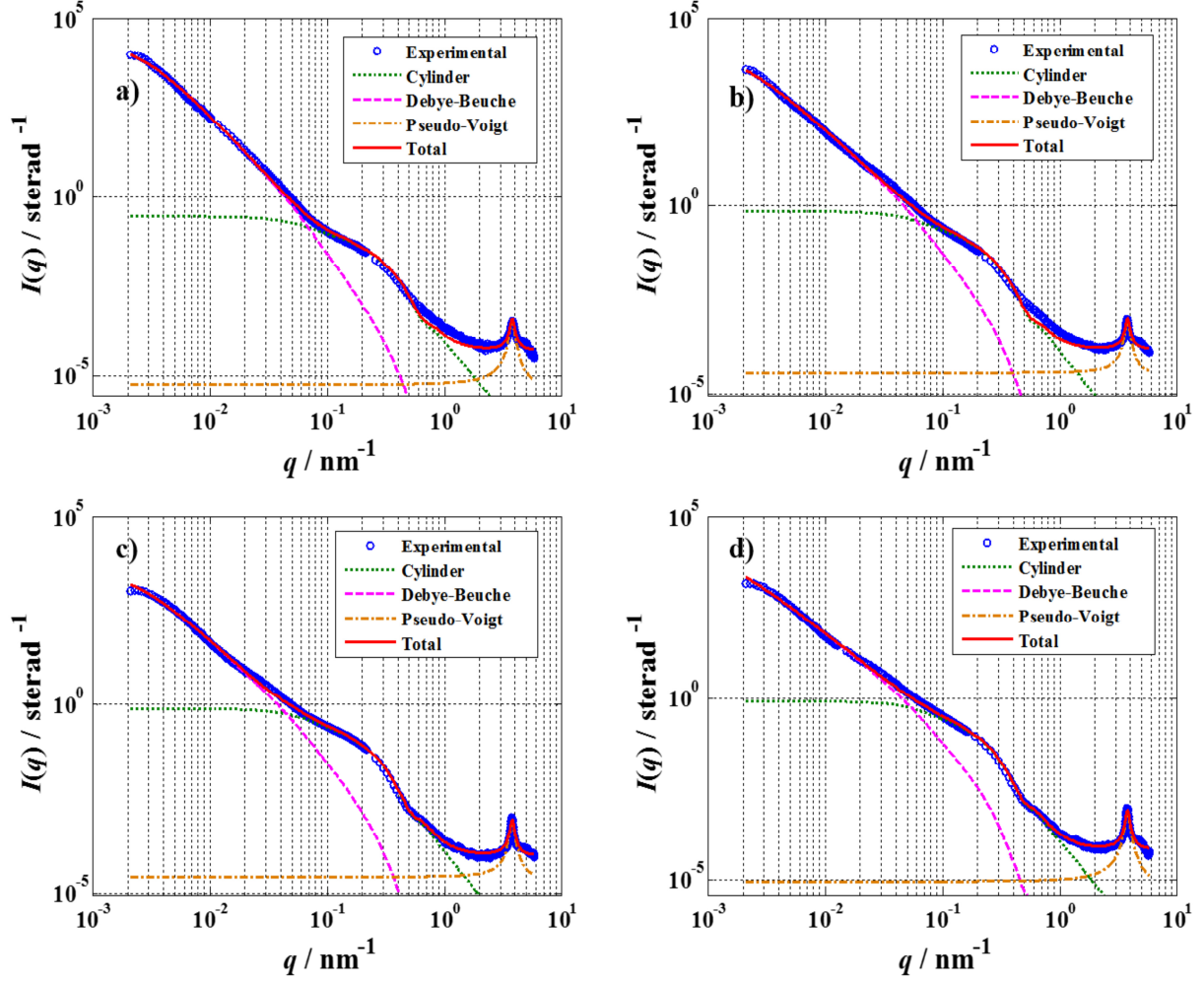


**Figure 2.** The SAXS modelling of experimental data for P3HT/PC<sub>61</sub>BM thin films isothermally annealed at 400 K for different duration of time. a) As-cast sample, b) 60 s, c) 720 s, and d) 7500 s.

Figure 2 presents the fitted SAXS profiles for the P3HT/PC<sub>61</sub>BM films. The global fits were performed using the SAXSutilities program<sup>50</sup> after refining the form factor model and parameters using the SASview analysis package.<sup>64</sup> The intermediate  $q$ -range is adequately described by the polydisperse cylinder model<sup>21</sup> which provided the mean particle radius ( $\bar{R}$ ) and height ( $\bar{H}$ ). In addition,  $S_p(q) \approx 1$ , since there is no clear interaction peak which might also be smeared by the

large size distribution of particles. For pure P3HT crystals, a better fit may be obtained with a parallelepiped shape<sup>37</sup> but the differences are small and within the uncertainties. The determination of mean height is more uncertain due to the cross-over to the low  $q$  power law region. Results are summarized in **Table 2**. The fit results indicate that the mean radius of the polymer particles is significantly larger in the presence of PC<sub>61</sub>BM (3.7 nm and 5.9 nm, respectively) and systematically increases from 6.9 nm (annealed for 60 s) to 7.8 nm (annealed for 7500 s) for isothermally annealed P3HT/PC<sub>61</sub>BM thin films at 400 K (see **Fig. 3a**). The mean height of the polymer particles remained nearly the same about 40 nm during the annealing process which is also comparable to the value for pure P3HT film. This implies a change in the aspect ratio by a factor 1.3. Overall the volume of the particles grew from about 4200 nm<sup>3</sup> (as cast film) to 7600 nm<sup>3</sup> for isothermally annealed P3HT/PC<sub>61</sub>BM thin films for 7500 s.

The scattering intensity at low  $q$  ( $< 2 \times 10^{-2} \text{ nm}^{-1}$ ) was fitted using the Debye-Beuche term which yielded information about the morphology and characteristic size of PC<sub>61</sub>BM domains. However, a clear Guinier region of these clusters was not captured by the  $q$  range of the measurement and therefore the resulting  $R_g$  should be considered as a lower limit. The power-law exponent ( $p$ ) decreased from 1.7 (as cast film) to 1.25 for isothermally annealed P3HT/PC<sub>61</sub>BM thin films for 7500 s at 400 K, indicating a ramification<sup>57, 65</sup> of the structure of these domains. The apparent  $R_g$  of PC<sub>61</sub>BM clusters increased from 936 nm (as-cast) to 1578 nm (annealed for 7500 s) for isothermally annealed P3HT/PC<sub>61</sub>BM thin films. The average size parameters for domains at low  $q$  ( $< 0.1 \text{ nm}^{-1}$ ) are provided in **Table 2**. The interpretation of the power-law exponent,  $p$ , is complicated by the sub-micron thickness of the films. For the size scales probed at ultra-low  $q$ , the reduced dimensionality may come into play. For a perfect two-dimensional system, the Porod behavior becomes  $q^{-3}$  instead of the conventional  $q^{-4}$ .<sup>66</sup> Therefore, a  $p$  value in the range of 1.5 (*i.e.*



$q^{-3}$ , cf. eq. 1) may be attributed to the reduced dimensionality of the system. The observed power-law of the clusters ( $p < 1.5$ ) then corresponds to surface fractal morphology or highly percolated clusters. In this respect, the complementary information from X-ray ptychography is crucial for the interpretation of the size and morphology of domains.

**Table 2.** The structural parameters extracted from polydisperse cylinder model and Debye-Beuche (DB) model fitting of scattering intensity profiles for the pure P3HT and thermally annealed P3HT/PC<sub>61</sub>BM thin films.

BHJ thin films	Model Parameters					
	Polydisperse Cylinder			Debye-Beuche		
	$\bar{R}$ (nm)	$\bar{H}$ (nm)	$\bar{D}$	$\xi$ (nm)	$p$	$R_g$ (nm)
Pure P3HT as-cast	3.69	42.3	0.2	292.5	1.4	599
P3HT/PCBM as-cast	5.87	39.2	0.2	414.5	1.7	936
P3HT/PCBM Isothermal 60 s	6.92	40.6	0.2	560.0	1.4	1148
P3HT/PCBM Isothermal 720 s	7.39	38.5	0.2	471.0	1.4	965
P3HT/PCBM Isothermal 7500 s	7.80	39.8	0.2	815.0	1.25	1578

Note:  $\bar{R}$  and  $\bar{H}$  are mean radius and height of cylinders,  $\bar{D}$  is polydispersity parameter,  $\xi$  is the correlation length proportional to the mean radius of gyration ( $R_g$ ) of PC<sub>61</sub>BM clusters, and  $p$  is the power-law exponent.

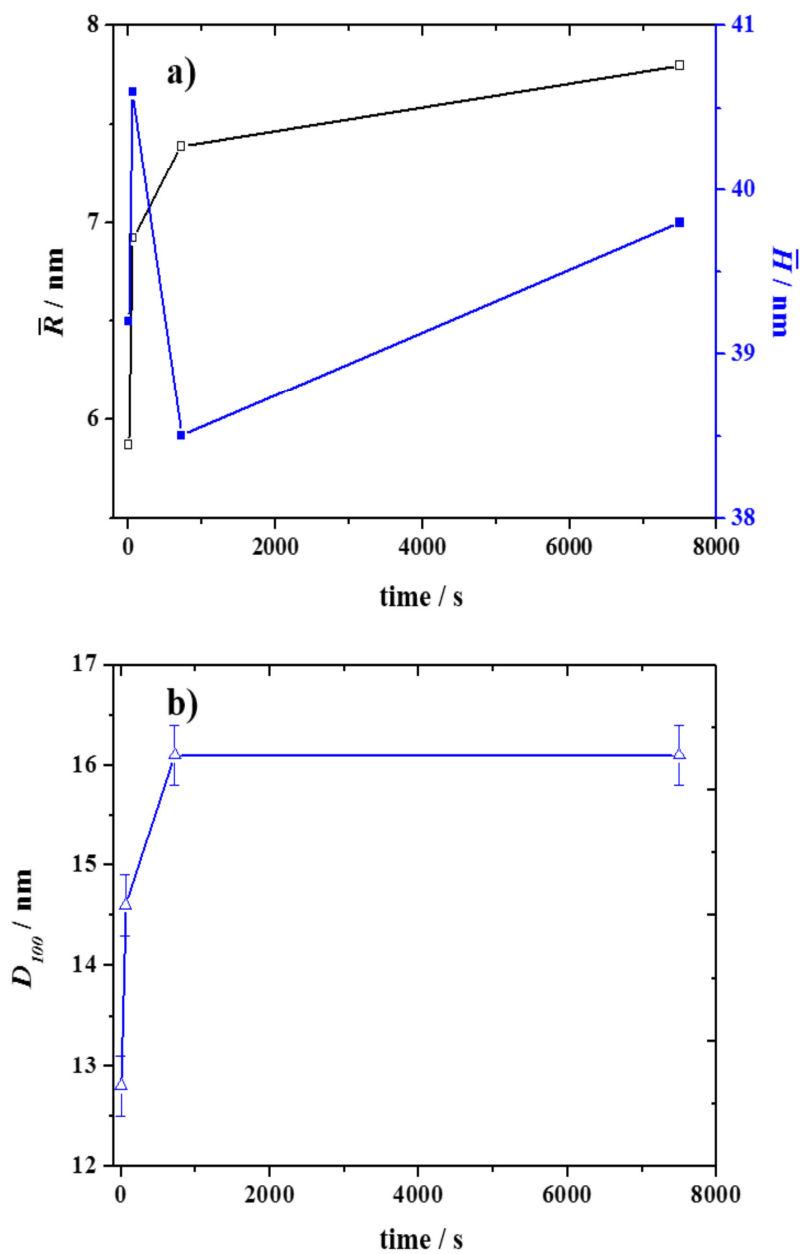


**Figure 3.** a) Mean radius ( $\bar{R}$ ), and height ( $\bar{H}$ ) of polymer particles, and b) The average thickness of P3HT lamellar crystals estimated from the Bragg peak at  $q \sim 3.8 \text{ nm}^{-1}$  using the Scherrer equation, as a function of thermal annealing times.

To complement the information deduced from the SAXS form factor analysis on the evolution of the P3HT crystallite size upon thermal annealing, the scattering intensity at high  $q$  ( $2.5\text{--}5.0\text{ nm}^{-1}$ ) was analyzed. For the as-cast film, the  $100$  peak at  $q_c \sim 3.82\text{ nm}^{-1}$  corresponds to the lamellar spacing  $d_{100} = 1.64\text{ nm}$  (see **Table 3**). The lamellar spacing increases slightly to  $1.66\text{ nm}$  ( $q_c \sim 3.77\text{ nm}^{-1}$ ) for isothermally annealed thin films due to thickening of lamellae. Using Scherrer's equation,<sup>67</sup>  $D_{hkl} = (K\lambda) / (\beta_{hkl} \cos\theta)$ , the average thickness  $D_{hkl}$  of the lamellar crystal was estimated from the peak widths ( $\beta_{hkl}$ ) of the  $100$  reflection with  $K \sim 1$ . An increase in the size of lamellar crystal from  $12.8\text{ nm}$  (as-cast) to  $16.1\text{ nm}$  for the thin film isothermally annealed for  $7500\text{ s}$  was obtained and can be attributed to a greater reorganization process as well as better ordering of polymer chains. The size of lamellar crystal for as cast thin film of P3HT was  $8.6\text{ nm}$  (see **Fig. 3b**). The constant lamellar spacing upon annealing suggests little incorporation of fullerene molecules into the crystalline lamellae, consistent with previous studies.<sup>25, 68</sup> The observed evolution of the lamellar crystal size is in good agreement with the mean radius of polymer particles presented in **Table 2**, confirming that the intermediate SAXS  $q$  range is dominated by scattering from the polymer particles.

**Table 3.** The parameters extracted from Pseudo-Voigt model fitting of the wide-angle Bragg peak appearing at  $q \sim 3.8 \text{ nm}^{-1}$ .

BHJ thin films	Model/Parameters			
	Pseudo-Voigt Model			
	$\sigma_L (\text{nm}^{-1})$	$\sigma_G (\text{nm}^{-1})$	$q_c (\text{nm}^{-1})$	$D_{hkl} (\text{nm})$
Pure P3HT as-cast	0.59	0.31	3.82	8.7
P3HT/PCBM as-cast	0.39	0.22	3.82	12.8
P3HT/PCBM Isothermal 60 s	0.38	0.15	3.78	14.6
P3HT/PCBM Isothermal 720 s	0.35	0.14	3.77	16.1
P3HT/PCBM Isothermal 7500 s	0.35	0.14	3.77	16.1

Note:  $\sigma_L$  and  $\sigma_G$  are width parameters for the Lorentzian and Gaussian terms,  $D_{hkl}$  is a thickness of crystal, and  $q_c$  is the scattering vector value at the peak position. The relative weighting factor,  $\mu = 0.5$  was used.

**3.2 Ptychographic phase-contrast imaging of thin film morphology.** Ptychography is a rapidly developing high-resolution imaging method based on coherent small-angle scattering and numerical phase retrieval,<sup>40-41, 69</sup> holding promise of future nanoscale imaging. Comparing the results obtained using ptychography to the USAXS data is thus of particular interest, as they are both fundamentally based on the same interaction of an X-ray beam probing the thin film sample in transmission geometry. To correlate the development of morphology traced through the SAXS/USAXS measurements, the samples were studied using 2D X-ray ptychographic imaging to directly image the thin film morphology. **Fig. 4** shows the resulting phase-contrast images of the thin films at room temperature. In our convention, larger *negative* phase shifts correspond to more strongly refracting materials. For presenting the ptychography images, the arbitrary reference

phase is chosen such that in all images zero corresponds to the lowest phase shift. Thus, under the assumption of a uniform sample thickness, darker regions have higher electron density as found in PC<sub>61</sub>BM-rich phases while lighter regions with lower electron density correspond to P3HT-rich phase respectively.<sup>33, 43-44</sup> The phase-contrast projections provided here are the only physical quantity that can be extracted without either invoking additional assumptions (e.g. constant thickness and an effectively 2D morphology, as reported in Patil et al.<sup>43</sup>), or tomographic 3D measurements. Still, the projections provide wide field-of-view images giving a high-resolution impression of the polymer morphology. Moreover, the ptychography projections are directly comparable to the USAXS measurements, as we will demonstrate.

The as-cast (60 s isothermally annealed) thin film sample shows the separated phases of PC<sub>61</sub>BM and polymer. Referring to the USAXS analysis in **section 3.1**, these separated phases can be assigned to the mixed phase domains of PC<sub>61</sub>BM clusters and polymer crystals in the amorphous matrix. The average size of these pure and mixed phases appears to be comparable to the values obtained from the USAXS analysis.

With further increase in isothermal annealing time to 720 s and 7500 s, the large domains of PC<sub>61</sub>BM clusters can be clearly noticed. (cf. **Fig. 4c** and **d**). The average size of PC<sub>61</sub>BM domains obtained from the USAXS analysis appears to be smaller compared to those observed in X-ray ptychography projections because the large scale domains (> 3  $\mu\text{m}$ ) cannot be detected by the accessible USAXS  $q$ -range in the present study.

Ptychography is widely considered the most promising method for large field-of-view high-resolution quantitative phase-contrast X-ray imaging. Note that for inorganic test samples resilient to radiation damage, the used 2D ptychography setup is able to reach a resolution of about 10 nm, one order of magnitude better than in the current study. As discussed in our previous publication

on 2D ptychography of P3HT/PC<sub>61</sub>BM,<sup>43</sup> going beyond a resolution of  $\sim 100$  nm proved difficult, and our understanding is that this limitation is set by radiation damage.

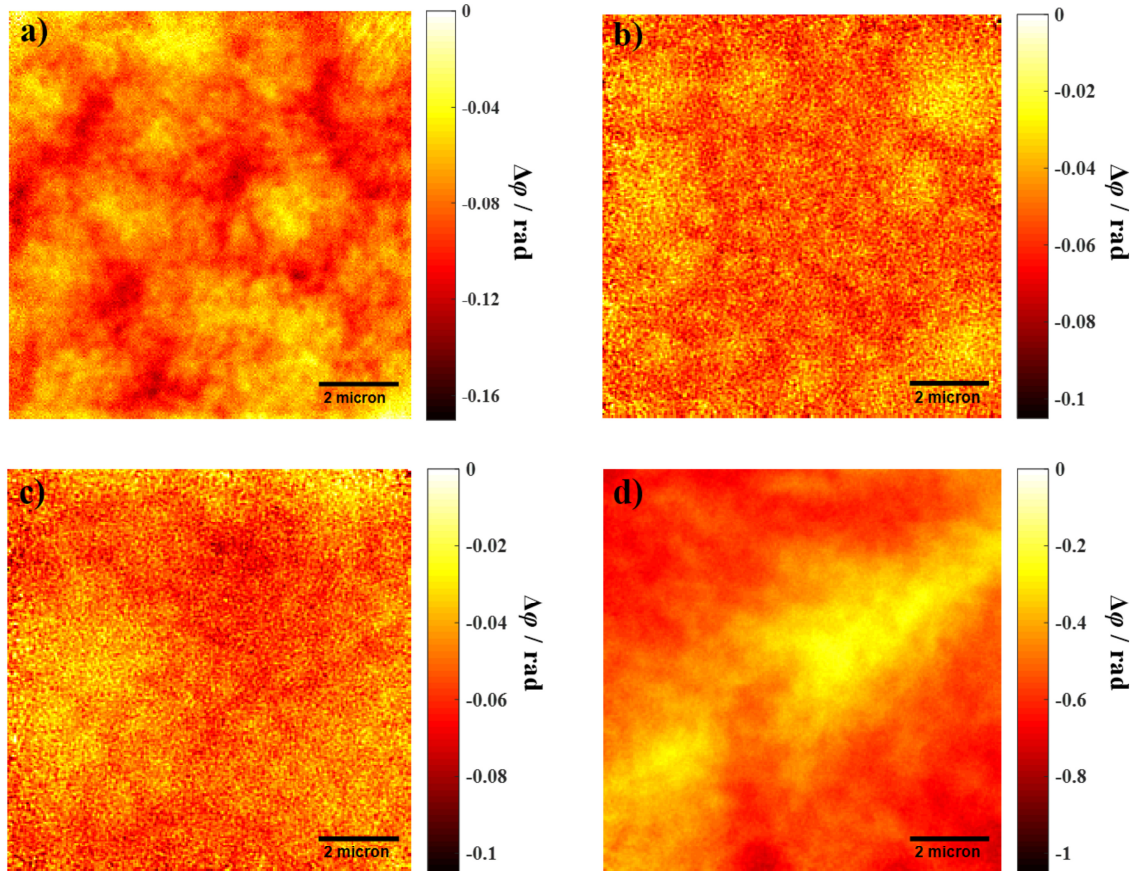


**Figure 4.** The reconstructed phase-contrast projections of P3HT/PC<sub>61</sub>BM thin films at room temperature showing the evolution of morphology for different annealing protocols. a) As-cast sample, b-d) after isothermal annealing treatment at 400 K with increasing annealing time of 60 s, 720 s and 7500 s. The scale on the colorbar represents the relative phase shift ( $\Delta\phi$ ).

**3.3 Comparison of scattering intensity from USAXS and X-ray ptychography.** It is instructive to compare the datasets obtained using SAXS and ptychography, because they are both collected with monochromatic X-rays of wavelength  $0.1 - 0.2$  nm at small scattering angles in a long sample-detector transmission geometry. However, one must recall that while USAXS data is collected with an essentially parallel beam, ptychography was performed with a pinhole giving a considerable beam divergence. Perhaps the most illustrative is the fact that in the absence of a sample, all the incoming radiation in the USAXS case would be stopped by the small central beamstop, whereas in the ptychography case, the radiation would be distributed across the detector<sup>70</sup>, and thus no beamstop is employed. The ptychographic dataset is effectively a convolution in the Fourier domain of the spatial-frequency, i.e. reciprocal-space, spectra of the object and illumination,<sup>71</sup> which makes comparing the detector signals not straightforward. However, the reconstruction from a ptychographic dataset effectively deconvolves the contributions of object and probe, which allows estimating the effective USAXS signal by calculating the absolute square of the discrete Fourier transform of the reconstructed object, and afterwards performing an azimuthal averaging, cf. **Fig. 5**.

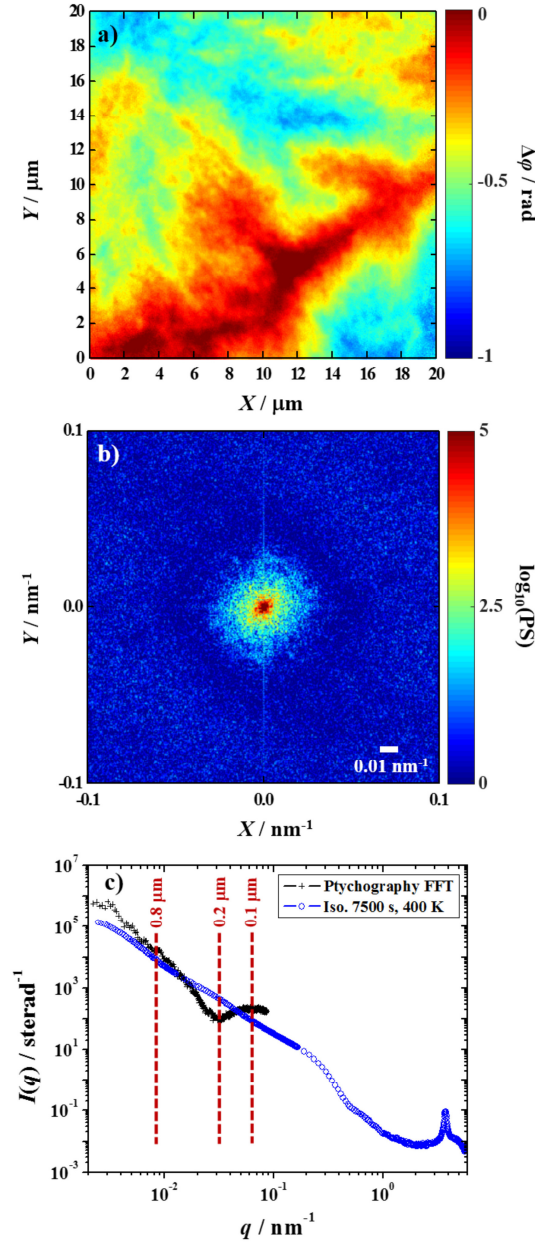


**Figure 5.** Comparison of USAXS and ptychography data for a P3HT/PC<sub>61</sub>BM thin film isothermally annealed for 7500 s at 400 K. a) High-resolution phase-contrast projection, and b) the corresponding Fast Fourier transform. c) Scattering intensity obtained from the ptychography image and USAXS measurements showing a similar trend in terms of Porod slopes below  $q = \sim 2 \times 10^{-2} \text{ nm}^{-1}$ .



For the lowest scattering vector values (say  $q < 2 \times 10^{-2} \text{ nm}^{-1}$ ) the ptychography dataset shows a similar (Porod) slope as the USAXS data. At larger  $q$ , corresponding to finer structural details in real space, there are large deviations (e.g. the minimum at  $0.03 \text{ nm}^{-1}$ ), as expected due to the estimated resolution being in the  $100 - 150 \text{ nm}$  range and because of the smaller statistical sampling in the ptychography experiment ( $\text{FOV} \sim 10 \mu\text{m} \times 10 \mu\text{m}$ ) compared to USAXS. Figure 5 thus highlights the relative strengths and complementarity of SAXS and ptychography. For  $q > 10^{-2} \text{ nm}^{-1}$  the SAXS signal outperforms ptychography, giving valuable nanoscale information. However, for the smallest  $q$  values, the USAXS data displays a rather featureless power-law which can be fitted with different structural models. In this range ptychography excels and provides unambiguous real-space structural information which could not be deduced from the USAXS data alone.

While ptychography with a resolution of  $\sim 10 \text{ nm}$  has been reported for inorganic materials,<sup>54, 72</sup> there are clear indications that radiation damage is a main limitation in achieving this performance with organic materials.<sup>43-44</sup> Corroborating both **Fig. 5** and previous reports, being able to push the ptychography measurements towards a spatial resolution  $\leq 10 \text{ nm}$  for organic materials would be the key to establishing ptychography as the method of choice for studying mesoscale structures in soft materials. The scattering-cross section of these films are relatively high and therefore it will be possible to investigate samples with thicknesses similar to those involved in real solar cells.

The combination of SAXS, USAXS, and X-ray ptychography provides a powerful way for real space and reciprocal space characterization of aggregate morphology also in many other systems, including block copolymers and star copolymers, of great interest to the polymer science community. For example, the miktoarm polymers, that are promising for drug delivery, are known

to aggregate into supramolecular assemblies, such as segmented ribbons and core-shell-corona micelles in solution, depending on external parameters including temperature, pH and choice of solvent. Therefore, the combined use of X-ray imaging and scattering techniques could provide better insight for the development of polymer therapeutics, including supramolecular drug delivery systems.

#### **4. CONCLUSIONS.**

In conclusion, we have studied the morphological variations in organic thin films with and without isothermal annealing treatment. The SAXS/USAXS experiments allowed probing the BHJ structure over a wide  $q$ -range which is not accessible using traditional SAXS techniques. We have introduced a simplified structural model with a minimum number of physically traceable parameters which can quantitatively describe the scattered intensity over the entire measured  $q$ -range. The USAXS experiments indicated a ramification of the domains of PC<sub>61</sub>BM when the thin film is subjected to the isothermal thermal annealing for longer times. These results are consistent with the X-ray ptychography measurements where the large aggregates are visible as indicated by the darker regions in the reconstructed 2D high-resolution phase-contrast images becoming more disperse. The comparison of scattering cross-section extracted from ptychographic phase contrast projection and USAXS data shows quantitative agreement in the region of overlap. These results further consolidate X-ray ptychography as a robust and complementary method to the USAXS technique in providing useful information about micron scale structures that are generally probed at low angles. The combination of these X-ray imaging and scattering techniques provides a practical way, through quantitative analysis in both real and reciprocal space, to deciphering

features of buried structures in functional assemblies – which is a topic of great importance in applied polymer science.

## **AUTHOR INFORMATION**

### **Corresponding Author**

\* (N.P.) E-mail: [nil.pat@gmail.com](mailto:nil.pat@gmail.com)

### **Author Contributions**

N.P. and D.W.B. designed the study. N.P., N.V.D.B., E.T.B.S., R.C., M.G.S. and D.W.B. performed the X-ray ptychography measurements. N.P., E.T.B.S. and D.W.B. analyzed the X-ray ptychography reconstructions. T.N. performed the SAXS/USAXS measurements. T. N., L.M. and N.P. analyzed the SAXS/USAXS data. N.V.D.B., R.C. and B.V.M. fabricated the organic thin films and carried out the thermal treatments. All authors contributed to the revision of the manuscript. N.P., D. W. B. and T.N. wrote the manuscript.

### **Notes**

The authors declare no competing financial interest.

## **ACKNOWLEDGEMENTS**

The authors thank The Research Council of Norway for financial support through the M-ERA.NET project “RADESOL” under the European Union’s seventh framework programme (FP/2007-2013), grant agreement no. 234648/O70. DWB thanks the Research Council of Norway through its Centres of Excellence funding scheme, project number 262644. Partial funding for this

research was obtained from the EU's seventh framework programme (FP7/2007-2013) under grant agreement no. 262348 (for ESMI), and from the Norwegian PhD Network on Nanotechnology for Microsystems, which is sponsored by the Research Council of Norway, Division for Science, contract no. 221860/F40. The USAXS experiments were carried out at the ID02 beamline of ESRF – the European Synchrotron, France. The ptychography experiments were done at cSAXS beamline, Swiss Light Source, Paul Scherrer Institut, Switzerland.

## REFERENCES

1. Sariciftci, N.; Smilowitz, L.; Heeger, A. J.; Wudl, F., Photoinduced electron transfer from a conducting polymer to buckminsterfullerene. *Science* **1992**, 258 (5087), 1474-1476.
2. Park, S. H.; Roy, A.; Beaupre, S.; Cho, S.; Coates, N.; Moon, J. S.; Moses, D.; Leclerc, M.; Lee, K.; Heeger, A. J., Bulk heterojunction solar cells with internal quantum efficiency approaching 100&percent. *Nature Photonics* **2009**, 3 (5), 297-302.
3. Noriega, R.; Rivnay, J.; Vandewal, K.; Koch, F. P.; Stingelin, N.; Smith, P.; Toney, M. F.; Salleo, A., A general relationship between disorder, aggregation and charge transport in conjugated polymers. *Nature Materials* **2013**, 12 (11), 1038-1044.
4. Coropceanu, V.; Cornil, J.; da Silva Filho, D. A.; Olivier, Y.; Silbey, R.; Brédas, J.-L., Charge transport in organic semiconductors. *Chemical Reviews* **2007**, 107 (4), 926-952.
5. Opitz, A.; Wagner, J.; Brütting, W.; Salzmann, I.; Koch, N.; Manara, J.; Pflaum, J.; Hinderhofer, A.; Schreiber, F., Charge separation at molecular donor–acceptor interfaces:

- correlation between morphology and solar cell performance. *IEEE Journal of Selected Topics in Quantum Electronics* **2010**, *16* (6), 1707-1717.
6. Shaw, P. E.; Ruseckas, A.; Samuel, I. D., Exciton diffusion measurements in poly (3-hexylthiophene). *Advanced Materials* **2008**, *20* (18), 3516-3520.
  7. Zhao, J.; Li, Y.; Yang, G.; Jiang, K.; Lin, H.; Ade, H.; Ma, W.; Yan, H., Efficient organic solar cells processed from hydrocarbon solvents. *Nature Energy* **2016**, *1*, 15027.
  8. Rivnay, J.; Mannsfeld, S. C.; Miller, C. E.; Salleo, A.; Toney, M. F., Quantitative determination of organic semiconductor microstructure from the molecular to device scale. *Chemical Reviews* **2012**, *112* (10), 5488-5519.
  9. Watts, B.; Belcher, W. J.; Thomsen, L.; Ade, H.; Dastoor, P. C., A quantitative study of PCBM diffusion during annealing of P3HT: PCBM blend films. *Macromolecules* **2009**, *42* (21), 8392-8397.
  10. Li, G.; Shrotriya, V.; Huang, J.; Yao, Y.; Moriarty, T.; Emery, K.; Yang, Y., High-efficiency solution processable polymer photovoltaic cells by self-organization of polymer blends. *Nature Materials* **2005**, *4* (11), 864-868.
  11. Treat, N. D.; Brady, M. A.; Smith, G.; Toney, M. F.; Kramer, E. J.; Hawker, C. J.; Chabinyc, M. L., Interdiffusion of PCBM and P3HT reveals miscibility in a photovoltaically active blend. *Advanced Energy Materials* **2011**, *1* (1), 82-89.
  12. Martens, T.; D'Haen, J.; Munters, T.; Beelen, Z.; Goris, L.; Manca, J.; D'Olieslaeger, M.; Vanderzande, D.; De Schepper, L.; Andriessen, R., Disclosure of the nanostructure of

MDMO-PPV: PCBM bulk hetero-junction organic solar cells by a combination of SPM and TEM. *Synthetic Metals* **2003**, *138* (1), 243-247.

13. Hoppe, H.; Niggemann, M.; Winder, C.; Kraut, J.; Hiesgen, R.; Hinsch, A.; Meissner, D.; Sariciftci, N. S., Nanoscale morphology of conjugated polymer/fullerene-based bulk-heterojunction solar cells. *Advanced Functional Materials* **2004**, *14* (10), 1005-1011.
14. Savenije, T. J.; Kroeze, J. E.; Yang, X.; Loos, J., The effect of thermal treatment on the morphology and charge carrier dynamics in a polythiophene–fullerene bulk heterojunction. *Advanced Functional Materials* **2005**, *15* (8), 1260-1266.
15. Campoy-Quiles, M.; Ferenczi, T.; Agostinelli, T.; Etchegoin, P. G.; Kim, Y.; Anthopoulos, T. D.; Stavrinou, P. N.; Bradley, D. D.; Nelson, J., Morphology evolution via self-organization and lateral and vertical diffusion in polymer: fullerene solar cell blends. *Nature Materials* **2008**, *7* (2), 158-164.
16. Kline, R. J.; McGehee, M. D.; Kadnikova, E. N.; Liu, J.; Fréchet, J. M.; Toney, M. F., Dependence of regioregular poly (3-hexylthiophene) film morphology and field-effect mobility on molecular weight. *Macromolecules* **2005**, *38* (8), 3312-3319.
17. Mena-Osteritz, E.; Meyer, A.; Langeveld-Voss, B. M.; Janssen, R. A.; Meijer, E.; Bäuerle, P., Two-Dimensional Crystals of Poly (3-Alkyl-thiophene) s: Direct Visualization of Polymer Folds in Submolecular Resolution. *Angewandte Chemie International Edition* **2000**, *39* (15), 2679-2684.

18. Grévin, B.; Rannou, P.; Payerne, R.; Pron, A.; Travers, J., Multi-scale scanning tunneling microscopy imaging of self-organized regioregular poly (3-hexylthiophene) films. *The Journal of Chemical Physics* **2003**, *118* (15), 7097-7102.
19. van Bavel, S.; Sourty, E.; de With, G.; Frolic, K.; Loos, J., Relation between photoactive layer thickness, 3D morphology, and device performance in P3HT/PCBM bulk-heterojunction solar cells. *Macromolecules* **2009**, *42* (19), 7396-7403.
20. Burke, K. B.; Stapleton, A. J.; Vaughan, B.; Zhou, X.; Kilcoyne, A. D.; Belcher, W. J.; Dastoor, P. C., Scanning transmission X-ray microscopy of polymer nanoparticles: Probing morphology on sub-10 nm length scales. *Nanotechnology* **2011**, *22* (26), 265710.
21. Pedersen, J. S., Analysis of small-angle scattering data from colloids and polymer solutions: modeling and least-squares fitting. *Advances in Colloid and Interface Science* **1997**, *70*, 171-210.
22. Sirringhaus, H.; Brown, P.; Friend, R.; Nielsen, M. M.; Bechgaard, K.; Langeveld-Voss, B.; Spiering, A.; Janssen, R. A.; Meijer, E.; Herwig, P., Two-dimensional charge transport in self-organized, high-mobility conjugated polymers. *Nature* **1999**, *401* (6754), 685-688.
23. Breiby, D. W.; Samuelsen, E. J.; Konovalov, O., The drying behaviour of conjugated polymer solutions. *Synthetic Metals* **2003**, *139* (2), 361-369.
24. Breiby, D. W.; Bunk, O.; Andreasen, J. W.; Lemke, H. T.; Nielsen, M. M., Simulating X-ray diffraction of textured films. *Journal of Applied Crystallography* **2008**, *41* (2), 262-271.
25. Müller-Buschbaum, P., The active layer morphology of organic solar cells probed with grazing incidence scattering techniques. *Advanced Materials* **2014**, *26* (46), 7692-7709.

26. Narayanan, T.; Sztucki, M.; Van Vaerenbergh, P.; Léonardon, J.; Gorini, J.; Claustre, L.; Sever, F.; Morse, J.; Boesecke, P., A multipurpose instrument for time-resolved ultra-small-angle and coherent X-ray scattering. *Journal of Applied Crystallography* **2018**, *51* (6), 1511-1524.
27. Liao, H.-C.; Tsao, C.-S.; Lin, T.-H.; Chuang, C.-M.; Chen, C.-Y.; Jeng, U.-S.; Su, C.-H.; Chen, Y.-F.; Su, W.-F., Quantitative nanoorganized structural evolution for a high efficiency bulk heterojunction polymer solar cell. *Journal of the American Chemical Society* **2011**, *133* (33), 13064-13073.
28. Kiel, J. W.; Eberle, A. P.; Mackay, M. E., Nanoparticle agglomeration in polymer-based solar cells. *Physical Review Letters* **2010**, *105* (16), 168701.
29. Wu, W.-R.; Jeng, U.-S.; Su, C.-J.; Wei, K.-H.; Su, M.-S.; Chiu, M.-Y.; Chen, C.-Y.; Su, W.-B.; Su, C.-H.; Su, A.-C., Competition between fullerene aggregation and poly (3-hexylthiophene) crystallization upon annealing of bulk heterojunction solar cells. *ACS Nano* **2011**, *5* (8), 6233-6243.
30. Kozub, D. R.; Vakhshouri, K.; Orme, L. M.; Wang, C.; Hexemer, A.; Gomez, E. D., Polymer crystallization of partially miscible polythiophene/fullerene mixtures controls morphology. *Macromolecules* **2011**, *44* (14), 5722-5726.
31. Yin, W.; Dadmun, M., A new model for the morphology of P3HT/PCBM organic photovoltaics from small-angle neutron scattering: rivers and streams. *ACS Nano* **2011**, *5* (6), 4756-4768.



32. Chen, W.; Xu, T.; He, F.; Wang, W.; Wang, C.; Strzalka, J.; Liu, Y.; Wen, J.; Miller, D. J.; Chen, J., Hierarchical nanomorphologies promote exciton dissociation in polymer/fullerene bulk heterojunction solar cells. *Nano Letters* **2011**, *11* (9), 3707-3713.
33. Chiu, M. Y.; Jeng, U.; Su, C. H.; Liang, K. S.; Wei, K. H., Simultaneous use of small-and wide-angle X-ray techniques to analyze nanometerscale phase separation in polymer heterojunction solar cells. *Advanced Materials* **2008**, *20* (13), 2573-2578.
34. Vajjala Kesava, S.; Dhanker, R.; Kozub, D. R.; Vakhshouri, K.; Choi, U. H.; Colby, R. H.; Wang, C.; Hexemer, A.; Giebink, N. C.; Gomez, E. D., Mesoscopic structural length scales in P3HT/PCBM mixtures remain invariant for various processing conditions. *Chemistry of Materials* **2013**, *25* (14), 2812-2818.
35. Huang, Y.-C.; Tsao, C.-S.; Cha, H.-C.; Chuang, C.-M.; Su, C.-J.; Jeng, U.-S.; Chen, C.-Y., Correlation between Hierarchical Structure and Processing Control of Large-area Spray-coated Polymer Solar Cells toward High Performance. *Scientific Reports* **2016**, *6*, 20062.
36. Chen, C.-Y.; Chan, S.-H.; Li, J.-Y.; Wu, K.-H.; Chen, H.-L.; Chen, J.-H.; Huang, W.-Y.; Chen, S.-A., Formation and thermally-induced disruption of nanowhiskers in poly (3-hexylthiophene)/xylene gel studied by small-angle x-ray scattering. *Macromolecules* **2010**, *43* (17), 7305-7311.
37. Newbloom, G. M.; Kim, F. S.; Jenekhe, S. A.; Pozzo, D. C., Mesoscale morphology and charge transport in colloidal networks of poly (3-hexylthiophene). *Macromolecules* **2011**, *44* (10), 3801-3809.

38. Ade, H.; Stoll, H., Near-edge X-ray absorption fine-structure microscopy of organic and magnetic materials. *Nature Materials* **2009**, 8 (4), 281-290.
39. McNeill, C. R.; Watts, B.; Thomsen, L.; Belcher, W. J.; Greenham, N. C.; Dastoor, P. C., Nanoscale quantitative chemical mapping of conjugated polymer blends. *Nano Letters* **2006**, 6 (6), 1202-1206.
40. Esmaeili, M.; Fløystad, J. B.; Diaz, A.; Høydalsvik, K.; Guizar-Sicairos, M.; Andreassen, J. W.; Breiby, D. W., Ptychographic X-ray tomography of silk fiber hydration. *Macromolecules* **2013**, 46 (2), 434-439.
41. Thibault, P.; Dierolf, M.; Menzel, A.; Bunk, O.; David, C.; Pfeiffer, F., High-resolution scanning x-ray diffraction microscopy. *Science* **2008**, 321 (5887), 379-382.
42. Rodenburg, J.; Hurst, A.; Cullis, A.; Dobson, B.; Pfeiffer, F.; Bunk, O.; David, C.; Jefimovs, K.; Johnson, I., Hard-x-ray lensless imaging of extended objects. *Physical Review Letters* **2007**, 98 (3), 034801.
43. Patil, N.; Skjønsvell, E. T. B.; Van den Brande, N.; Panduro, E. A. C.; Claessens, R.; Guizar-Sicairos, M.; Van Mele, B.; Breiby, D. W., X-Ray Nanoscopy of a Bulk Heterojunction. *PLOS ONE* **2016**, 11 (7), e0158345.
44. Van den Brande, N.; Patil, N.; Guizar-Sicairos, M.; Claessens, R.; Van Assche, G.; Breiby, D.; Van Mele, B., Probing the bulk heterojunction morphology in thermally annealed active layers for polymer solar cells. *Organic Electronics* **2017**, 41, 319-326.
45. Bø Fløystad, J.; Skjønsvell, E. T. B.; Guizar-Sicairos, M.; Høydalsvik, K.; He, J.; Andreassen, J. W.; Zhang, Z.; Breiby, D. W., Quantitative 3D X-ray Imaging of Densification,

- Delamination and Fracture in a Micro-Composite under Compression. *Advanced Engineering Materials* **2015**, *17* (4), 545-553.
46. Høydalsvik, K.; Bø Fløystad, J.; Zhao, T.; Esmaili, M.; Diaz, A.; Andreasen, J. W.; Mathiesen, R. H.; Rønning, M.; Breiby, D. W., In situ X-ray ptychography imaging of high-temperature CO<sub>2</sub> acceptor particle agglomerates. *Applied Physics Letters* **2014**, *104* (24), 241909.
47. Pedersen, E. B. L.; Angmo, D.; Dam, H. F.; Thydén, K. T. S.; Andersen, T. R.; Skjønsvell, E. T. B.; Krebs, F. C.; Holler, M.; Diaz, A.; Guizar-Sicairos, M., Improving organic tandem solar cells based on water-processed nanoparticles by quantitative 3D nanoimaging. *Nanoscale* **2015**, *7* (32), 13765-13774.
48. Guizar-Sicairos, M.; Fienup, J. R., Phase retrieval with transverse translation diversity: a nonlinear optimization approach. *Optics Express* **2008**, *16* (10), 7264-7278.
49. Maiden, A. M.; Rodenburg, J. M., An improved ptychographical phase retrieval algorithm for diffractive imaging. *Ultramicroscopy* **2009**, *109* (10), 1256-1262.
50. Sztucki, M.; Narayanan, T., Development of an ultra-small-angle X-ray scattering instrument for probing the microstructure and the dynamics of soft matter. *Applied Crystallography* **2007**, *40* (s1), s459-s462.
51. Henrich, B.; Bergamaschi, A.; Broennimann, C.; Dinapoli, R.; Eikenberry, E.; Johnson, I.; Kobas, M.; Kraft, P.; Mozzanica, A.; Schmitt, B., PILATUS: A single photon counting pixel detector for X-ray applications. *Nuclear Instruments and Methods in Physics Research*

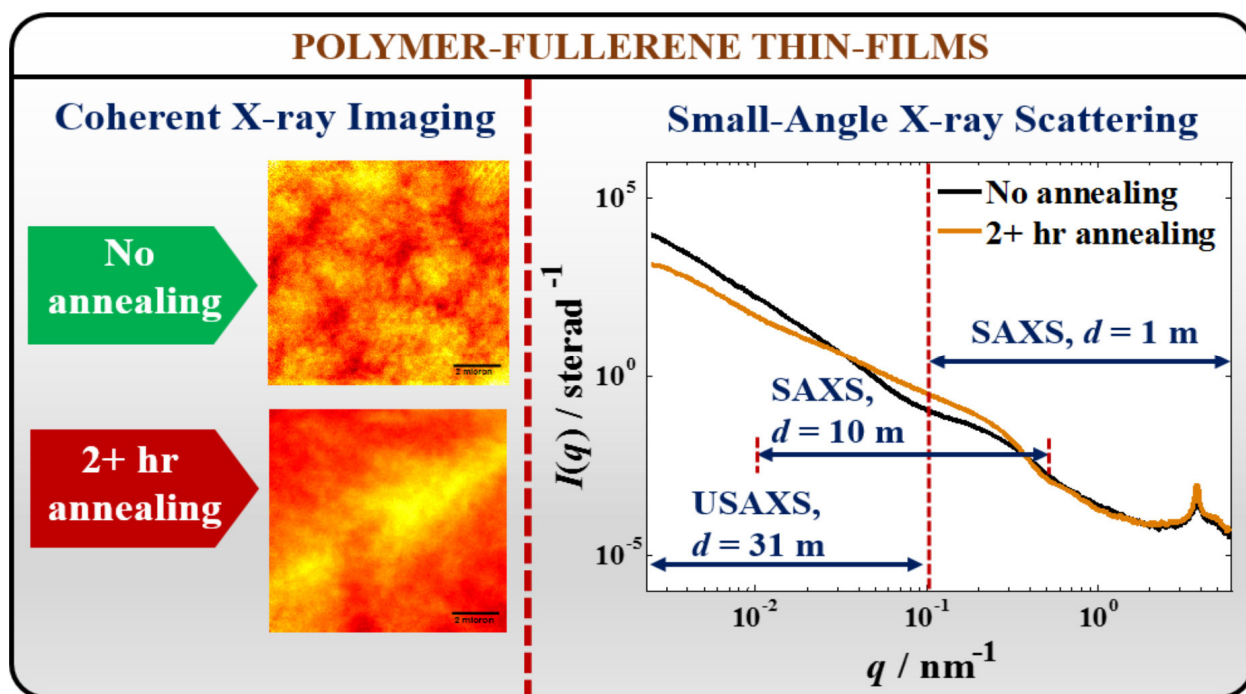
*Section A: Accelerators, Spectrometers, Detectors and Associated Equipment* **2009**, 607 (1), 247-249.

52. Huang, X.; Yan, H.; Harder, R.; Hwu, Y.; Robinson, I. K.; Chu, Y. S., Optimization of overlap uniformness for ptychography. *Optics Express* **2014**, 22 (10), 12634-12644.
53. Guizar-Sicairos, M.; Diaz, A.; Holler, M.; Lucas, M. S.; Menzel, A.; Wepf, R. A.; Bunk, O., Phase tomography from x-ray coherent diffractive imaging projections. *Optics Express* **2011**, 19 (22), 21345-21357.
54. Vila-Comamala, J.; Diaz, A.; Guizar-Sicairos, M.; Manton, A.; Kewish, C. M.; Menzel, A.; Bunk, O.; David, C., Characterization of high-resolution diffractive X-ray optics by ptychographic coherent diffractive imaging. *Optics Express* **2011**, 19 (22), 21333-21344.
55. Van Heel, M.; Schatz, M., Fourier shell correlation threshold criteria. *Journal of Structural Biology* **2005**, 151 (3), 250-262.
56. Kohn, P.; Rong, Z.; Scherer, K. H.; Sepe, A.; Sommer, M.; Müller-Buschbaum, P.; Friend, R. H.; Steiner, U.; Hüttner, S., Crystallization-induced 10-nm structure formation in P3HT/PCBM blends. *Macromolecules* **2013**, 46 (10), 4002-4013.
57. Narayanan, T., Small-Angle Scattering. *Structure from diffraction methods* **2014**, 259-324.
58. Samuelsen, E.; Mårdalen, J., The Structure of Polythiophenes. Wiley: New York: 1997; Vol. 3, pp 87-120.
59. Fell, H.; Samuelsen, E.; Als-Nielsen, J.; Grübel, G.; Mårdalen, J., Unexpected orientational effects in spin-cast, sub-micron layers of poly (alkylthiophene) s: A diffraction study with synchrotron radiation. *Solid State Communications* **1995**, 94 (10), 843-846.

60. Breiby, D. W.; Samuelsen, E. J., Quantification of preferential orientation in conjugated polymers using X-ray diffraction. *Journal of Polymer Science Part B: Polymer Physics* **2003**, *41* (20), 2375-2393.
61. Gomez, E. D.; Barteau, K. P.; Wang, H.; Toney, M. F.; Loo, Y.-L., Correlating the scattered intensities of P3HT and PCBM to the current densities of polymer solar cells. *Chemical Communications* **2011**, *47* (1), 436-438.
62. Debye, P.; Bueche, A., Scattering by an inhomogeneous solid. *Journal of Applied Physics* **1949**, *20* (6), 518-525.
63. Wertheim, G.; Butler, M.; West, K.; Buchanan, D., Determination of the Gaussian and Lorentzian content of experimental line shapes. *Review of Scientific Instruments* **1974**, *45* (11), 1369-1371.
64. Alina, G.; Butler, P.; Cho, J.; Doucet, M.; Kienzle, P., SASView for Small Angle Scattering Analysis. 2017.
65. Beaucage, G., Determination of branch fraction and minimum dimension of mass-fractal aggregates. *Physical Review E* **2004**, *70* (3), 031401.
66. Oono, Y.; Puri, S., Large wave number features of form factors for phase transition kinetics. *Modern Physics Letters B* **1988**, *2* (07), 861-867.
67. Scherrer, P., Zsigmondy's Kolloidchemie. *Nachrichten der Göttinger Gesellschaft* **1918**, *98*, 394.
68. Mayer, A.; Toney, M. F.; Scully, S. R.; Rivnay, J.; Brabec, C. J.; Scharber, M.; Koppe, M.; Heeney, M.; McCulloch, I.; McGehee, M. D., Bimolecular crystals of fullerenes in

- conjugated polymers and the implications of molecular mixing for solar cells. *Advanced Functional Materials* **2009**, *19* (8), 1173-1179.
69. Faulkner, H.; Rodenburg, J., Movable aperture lensless transmission microscopy: a novel phase retrieval algorithm. *Physical Review Letters* **2004**, *93* (2), 023903.
70. Guizar-Sicairos, M.; Holler, M.; Diaz, A.; Vila-Comamala, J.; Bunk, O.; Menzel, A., Role of the illumination spatial-frequency spectrum for ptychography. *Physical Review B* **2012**, *86* (10), 100103.
71. McCallum, B.; Rodenburg, J., Two-dimensional demonstration of Wigner phase-retrieval microscopy in the STEM configuration. *Ultramicroscopy* **1992**, *45* (3-4), 371-380.
72. Holler, M.; Guizar-Sicairos, M.; Tsai, E. H.; Dinapoli, R.; Müller, E.; Bunk, O.; Raabe, J.; Aeppli, G., High-resolution non-destructive three-dimensional imaging of integrated circuits. *Nature* **2017**, *543* (7645), 402-406.

## TABLE OF CONTENTS



## SYNOPSIS:

Small-angle and ultra-small-angle X-ray scattering (SAXS and USAXS, respectively), and X-ray ptychographic microscopy were combined to study the mesoscale morphologies in thermally annealed thin films of P3HT/PC<sub>61</sub>BM blends over an unprecedentedly wide  $q$ -range.